Wide-range non-contact fluorescence intensity ratio thermometer based on Yb^{3+}/Nd^{3+} co-doped La_2O_3 microcrystals operating from 290 to 1230 K†

Guojun Gao, *[a] Dmitry Busko,[a] Sandra Kauffmann Weiss, [b] Andrey Turshatov, [a] Ian A. Howard [ac] and Bryce S. Richards *[ac]

Non-contact ratiometric thermometry has applications ranging from *in situ* physiological measurements to industrial process monitoring. The technique is based on the optical detection of the fluorescence intensity ratio (FIR) of two thermally-coupled levels (TCLs). Here, we report a Yb^{3+}/Nd^{3+} co-doped La_2O_3 microcrystal ratiometric thermometer based on upconverted emission in the near-infrared (NIR) after excitation with a 980 nm laser diode, which operates effectively over the wide temperature range from 290 1230 K. The thermometer uses the TCLs of Nd^{3+}:$^4F_{7/2}$ (emission peak 762 nm) and Nd^{3+}:$^4F_{5/2}$ (emission peak 825 nm). The chosen levels combine desirable characteristics to act as a sensitive temperature sensor over a wide range of elevated temperatures: namely a suitable energy gap (ΔE = 950 cm ^{1}); and weak thermal quenching effects (maximum photoluminescence at 803 and 853 K respectively for two Nd^{3+} emission peaks). This leads to a high relative sensitivity (S_R) of $1334/T^2$, and low temperature uncertainty ΔT_{min} of 0.1 K (<400 K), 1 K (400 853 K) and 3 K (853 1233 K). In addition to these characteristics, the excellent repeatability of FIR of the two Nd^{3+} emission peaks makes Yb^{3+}/Nd^{3+} co-doped La_2O_3 microcrystals a promising non-contact NIR ratiometric thermometer for temperatures up to 1230 K.

1. Introduction

Real-time temperature detection plays an important role in industry, manufacturing, climatology, scientific research, and other diverse applications.[1–5] Non-contact ratiometric thermometers based on fluorescence intensity ratio (FIR) of two thermally coupled levels (TCLs) are being rapidly developed and applied.[1–8] Compared with the traditional contact methods, these have many advantages such as no direct contact being required, self-referencing, high spatial resolution, high detection sensitively, rapid response and non-invasive operation.[1–7] The design of new luminescent materials with tailored emission properties is highly desired for the future development of non-contact ratiometric thermometers. For FIR- based thermometers, the two signals emitted from the TCL should significantly vary with temperature. The energy gap (ΔE) between two TCLs should be in the range of 200–2000 cm^{-1}.[9] TCLs with too small ΔE ($\Delta E < 200\ cm^{-1}$) will lead to strong overlap of signals, while too large ΔE value ($\Delta E > 2000\ cm^{-1}$) will result in the weak coupling of TCLs.[10] Many rare earth ions (such as Eu^{3+}, Tb^{3+}, Dy^{3+}, Er^{3+}, Nd^{3+}, Tm^{3+} and Ho^{3+}) have TCLs that make them promising for the FIR thermometry.[11–25]

Up-conversion (UC) refers to the phenomenon of converting two or more low energy photons into a high energy photon emission.[26–35] Yb^{3+}/Er^{3+} co-doped UC materials have been frequently reported as promising candidates for ratiometric thermometers.[26–31] Alternatively, Yb^{3+}/Nd^{3+} co-doped UC materials have been recently proposed as a novel promising candidate for ratiometric thermometer.[23,24,36–42] This is due to, firstly, Nd^{3+} possessing two sets of TCLs of $^4F_{7/2}/^4F_{5/2}$ and $^4F_{5/2}/^4F_{3/2}$, both of which possess an energy gap of $\sim$1000 cm^{-1}, thus making them highly suitable as ratiometric thermometers. Secondly, the UC emission bands of Nd^{3+} (750–950 nm) and excitation source (such as a 980 nm laser diode (LD)) are located in the first biological window (650–1000 nm), indicating great potential for biological applications.[13,23,43] Thirdly, the relatively cheap price of silicon charge-coupled detectors (CCD) and 980 nm

[a] *Institute of Microstructure Technology, Karlsruhe Institute of Technology, 76344 Eggenstein Leopoldshafen, Germany. E mail: guojun.gao@kit.edu, bryce.richards@kit.edu*
[b] *Institute of Technical Physics, Karlsruhe Institute of Technology, 76344 Eggenstein Leopoldshafen, Germany*
[c] *Light Technology Institute, Karlsruhe Institute of Technology, Engesserstrasse 13, 76131 Karlsruhe, Germany*

† Electronic supplementary information (ESI) available. See DOI: 10.1039/c8tc00782a

LD presents no barrier to large-scale and low-cost system realisation.[26,39] Lastly, the UC emission of Nd^{3+} in Yb^{3+}/Nd^{3+} co-doped phosphors exhibits only very weak thermal quenching, allowing bright luminescence even at elevated temperatures. This underpins their wide potential temperature sensing range. However, the present literature on Yb^{3+}/Nd^{3+} co-doped materials for NIR ratiometric thermometers has only reported relatively low temperature ranges, such as in $CaWO_4$:Yb^{3+},Nd^{3+} (303–873 K)[39] and $NaYF_4$:Yb^{3+},Nd^{3+} (297–453 K).[40]

Our recent study reveals that trigonal La_2O_3 micro-crystals are an excellent host material for rare earth ions due to their low phonon energy ($\sim$450 cm^{-1}) and low site symmetry (C_{3v} symmetry).[44] In this study, we choose La_2O_3 micro-crystals as the host materials for the Yb^{3+}/Nd^{3+} UC pair. The energy gap ΔE value of TCLs of $^4F_{7/2}$ (NIR1) and $^4F_{5/2}$ (NIR2) in La_2O_3 is determined to be 950 cm^{-1} which is highly suitable for ratiometric thermometers. The emission intensity of the NIR1 and NIR2 peaks strongly increases with temperatures up to 850 and 893 K, respectively. The weak thermal quenching and high temperature of the maximum UC emission for TCLs of NIR1 and NIR2 enable the high accuracy and temperature sensing over a wide temperature range. The combined features of high relative sensitivity (S_R) of $1334/T^2$ for Yb^{3+}/Nd^{3+}-based UC thermometers, excellent repeatability of NIR1 and NIR2, and FIR of NIR1/NIR2 indicated by four complete heating and cooling cycles, and low temperature uncertain ΔT_{min} of 0.1 K ($<$400 K) make them promising as ratiometric thermometers over a wide temperature range up to 1230 K.

2. Experimental

Sample preparation

A high temperature solid-state reaction was used to synthesize the micro-crystalline sample with nominal composition of $La_{1.86}O_3$:$1Nd^{3+}$,$6Yb^{3+}$. High purity La_2O_3 (99.9%, Chempur), Nd_2O_3 (99.9%, Chempur) and Yb_3O_3 (99.9%, Chempur) were used as the raw materials without further purification. A stoichiometric batch of 5 g starting materials was thoroughly mixed in an agate mortar and then sintered in an alumina crucible in a bottom-loading furnace (Carbolite BLF 1700) at 1550 °C for 24 h in ambient conditions with two intermediate grinding steps.

Characterization details

The phase purity of the micro-crystal was examined by X-ray diffractometry (XRD, Bruker, D8 phase, Cu Kα radiation) with a step width of 0.01° s^{-1} and a counting time of 1 s per step. Diffuse reflectance spectra (DRS) in the spectral region of 400–1050 nm was recorded with a spectrophotometer (Perkin-Elmer Lambda 950) equipped with an integrating sphere. The temperature dependent UC emission spectra in the temperature range of 293–1233 K were measured in a home-built optical system. A 980 nm continuous-wave LD (L980P200, Thorlabs Inc., max 200 mW) was used as the excitation source. The working temperature of LD was set at 293 K by a temperature controller (ITC4001, Thorlabs Inc.). The power density of LD was set at 1 W cm^{-2}. CCD spectrometer (AvaSpec-2048L-USB2, Avantes) was used as the detector to record the UC emission spectra.

Thermometry experiments were conducted as follows

The $La_{1.86}O_3$:$1Nd^{3+}$,$6Yb^{3+}$ micro-crystals were placed inside a thermal stage (Microptik BV, MHS1200-V/G) where the temperature was controlled in the range of 293–1233 K by a type S Pt-10% Rh/Pt thermocouple connected to a high performance temperature controller (Microptik BV, MTDC600) with a temperature resolution and accuracy of $\pm$0.1 K. The samples were held at the given temperature for 5 min to let the sample fully equilibrate and then we performed the UC measurement at the given temperature. The pump LD was turned on for a minimum time during the measurements to avoid any laser-related heating. To be precise, it was turned on just before each measurement, stabilized for 3 seconds, an UC measurement was taken over the next 1 second, and then it was turned off. A new background reading was taken for every temperature to avoid the potential interference of blackbody radiation. For the power dependent UC emission property, the power density of the laser beam was adjusted by the use of the controlled rotatable neutral density filter (Thorlabs) from 0.1 to 6 W cm^{-2}.

3. Results and discussion

Fig. 1a and b show the XRD and corresponding Rietveld analysis of La_2O_3:$6Yb^{3+}$,$1Nd^{3+}$, respectively. The crystal structure of La_2O_3 adopts the typical trigonal C-type structure of Ln_2O_3 (lanthanides, space group: $P\bar{3}m1$ (164); ICSD No.: 100204). Its crystal structure is composed of seven-fold coordinated [LaO_7] polyhedrons.[45] Compared with the undoped reference, the co-doping of small amounts of Yb^{3+}/Nd^{3+} (6/1 mol%) in La_2O_3 leads to the shift of all diffraction peaks of La_2O_3 to higher angles, indicating the incorporation of Yb^{3+} and Nd^{3+} in La_2O_3 lattice. The ionic radius of Yb^{3+} (0.925 Å in seven-fold coordination) is $\sim$19% smaller than that of La^{3+} (1.10 Å in seven-fold coordination).[46] The displacement of La^{3+} cites *via* smaller Yb^{3+} and Nd^{3+} ions will result in the contraction of the unit cell of La_2O_3. According to the well-known Bragg law of $n\lambda = 2d\sin(\theta)$, this will shift the diffraction peaks to higher angles. Additionally, the minor crystal phase of $LaYbO_3$ (space group: *Pna*21 (33); ICSD No.: 15093) can also observed. This is ascribed to the large ionic difference between Yb^{3+} and La^{3+} ($\sim$19%), which results in the low solubility of Yb^{3+} in La_2O_3 crystal phase. Thus, the high doping concentration of Yb^{3+} (6 mol%) leads to phase separation and the formation of perovskite-type $LaYbO_3$. This Yb^{3+} solubility issue here is also consistent with our former study on La_2O_3:Yb^{3+},Er^{3+} phosphors.[44] The formation of trace amounts of $LaYbO_3$ will weaken the UC performance of La_2O_3:Yb^{3+},Nd^{3+} due to the high possibility of the formation of Yb^{3+} ion clusters in $LaYbO_3$.

Fig. 1c shows a SEM image of La_2O_3:$6Yb^{3+}$,$1Nd^{3+}$. The morphology of La_2O_3:$6Yb^{3+}$,$1Nd^{3+}$ is irregularly shaped micron-scale particles with size of 1–5 μm. These particles tend to aggregate into bigger particles of 10–30 μm.

Fig. 1d presents the DRS of La_2O_3:$6Yb^{3+}$,$1Nd^{3+}$ in the spectral region of 400–1050 nm. The broad absorption bands

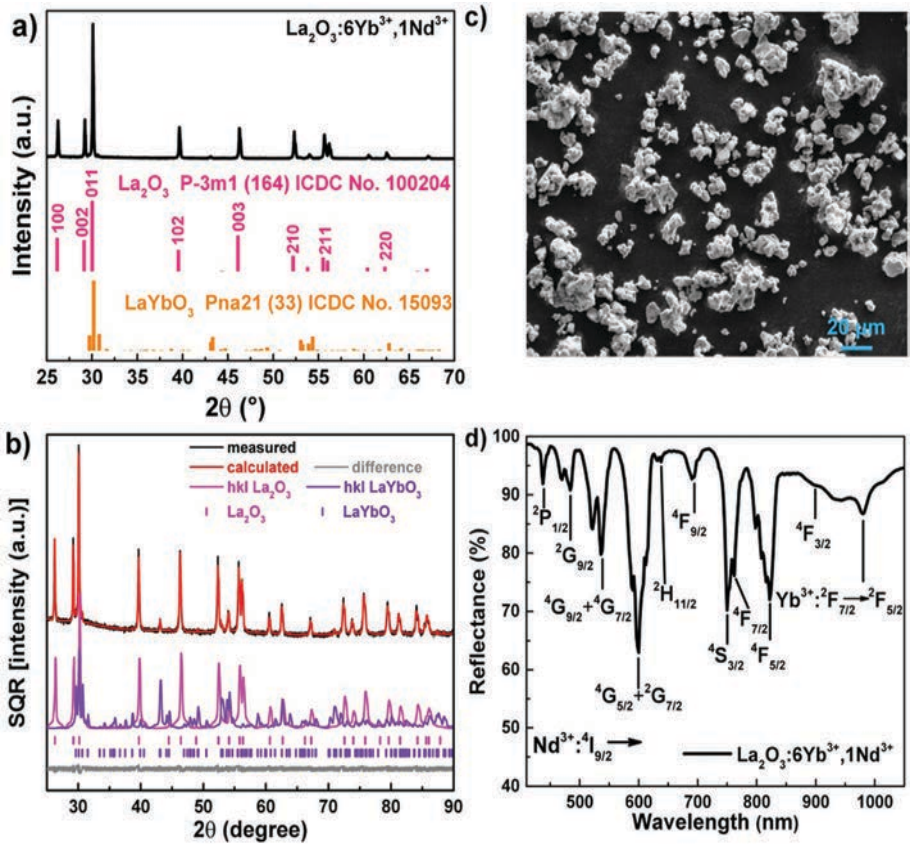

Fig. 1 (a) Power XRD pattern of La_2O_3:6Yb^{3+},1Nd^{3+} and tabulated standard diffraction patterns of trigonal La_2O_3 (pink) and $LaYbO_3$ (orange). (b) Rietveld analysis of La_2O_3:6Yb^{3+},1Nd^{3+}. (c) SEM image of La_2O_3:6Yb^{3+},1Nd^{3+} with magnification of ×1000. (d) Diffuse reflectance spectrum (DRS) of La_2O_3:6Yb^{3+},1Nd^{3+}. Labels in (d): the electronic transitions of Nd^{3+} and Yb^{3+} from ground state $^4I_{9/2}$ and $^2F_{7/2}$ to the labelled excited energy levels, respectively.

from 900–1050 nm with a sharp peak at ~980 nm and a broad shoulder at ~938 nm can be readily assigned to the electronic transitions of Yb^{3+} from the ground state of $^2F_{7/2}$ to excited state multiplet of $^2F_{5/2}$.[47–49] The absorption bands with maxima at ~900, 822, 762, 750, 690, 638, 600, 536, 484 and 438 nm are attributed to the absorption of Nd^{3+}. These are attributed to the electronic transitions of Nd^{3+} from the ground state $^4I/_{9/2}$ to the excited states of $^4F_{3/2}$, $^4F_{5/2}$, $^4S_{3/2}$, $^4F_{7/2}$, $^4F_{9/2}$, $^2H_{11/2}$, $^4G_{5/2}$ + $^2G_{7/2}$, $^4G_{9/2}$ + $^4G_{7/2}$, $^2G_{9/2}$ and $^2P_{1/2}$, respectively, as labelled in Fig. 1d. Remarkably, the strong overlap between absorption bands of Yb^{3+}:$^2F_{7/2}$ → $^2F_{5/2}$ and Nd^{3+}:$^4I/_{9/2}$ → $^4F_{3/2}$ at ~900 nm can be observed in Fig. 1d. According to the absorption peak value in Fig. 1d, the energy gap (ΔE) of TCLs of $^4F_{3/2}/^4F_{5/2}$, $^4F_{5/2}/^4F_{7/2}$ and $^4F_{3/2}/^4F_{7/2}$ is determined to be 1054, 958 and 2012 cm^{-1}, respectively. As indicated in introduction, the ΔE value of $^4F_{3/2}/^4F_{7/2}$ (>2000 cm^{-1}) is too big and leads to very weak thermal coupling between these two levels, which rules out its application. Additionally, the emission band of $^4F_{3/2}$ (~900 nm) strongly overlaps the thermally-stimulated UC emission of Yb^{3+}, which is frequently used for laser cooling.[50,51] The signal interference between Yb^{3+} and Nd^{3+} makes the emission band from Nd^{3+}:$^4F_{3/2}$ not suitable for the ratiometric thermometer study. Thus, only the TCLs of $^4F_{5/2}/^4F_{7/2}$ is considered for the ratiometric thermometer study in present study. The ΔE value of TCLs of $^4F_{7/2}/^4F_{5/2}$ is ~950 cm^{-1}, which is highly suitable for ratiometric thermometers.

Fig. 2a and b illustrate the UC emission spectra of La_2O_3:6Yb^{3+},1Nd^{3+} as a function of temperature from 293 to 833 and 833 to 1233 K, respectively. The excitation source is a 980 nm LD with a relatively low power density of 1 W cm^{-2}. The emission profile of Nd^{3+} spans a very broad spectral region from 730 to 855 nm, which are located in the first biological window (650–1000 nm).[42] More specifically, it is composed of two distinct bands: (i) 730–785 nm with maxima at 762 nm (defined as NIR1); and (ii) 785–855 nm with a maximum at 825 nm (defined as NIR2). They are assigned to the electronic transitions of Nd^{3+} from excited states of $^4F_{7/2}$ and $^4F_{5/2}$ to the ground state of $^4I_{9/2}$, respectively. As expected, no luminescence can be observed for Nd^{3+} singly doped sample upon excitation with the 980 nm LD.

As shown in Fig. 2c (magnified by ×200), faint UC emission bands with maximum at ~692, 638 and 613 nm appears with temperature >593 K due to the thermal population (TP) between $^4F_{7/2}$ with higher lying levels of Nd^{3+}. They are assigned to the transitions of Nd^{3+} from the excited levels of $^4F_{9/2}$, $^2H_{11/2}$ and $^4G_{5/2}$ to the ground state of $^4I_{9/2}$, respectively (Fig. 2e). Although there is thermal coupling of these levels with $^4F_{7/2}$, their extremely weak intensity rules out their real application in ratiometric thermometers.

Fig. 2d presents double-logarithmic plot of the variation of UC emission intensity at 825 nm (NIR2) with excitation power density ranging from 0.1–6 W cm^{-2}. In low power density

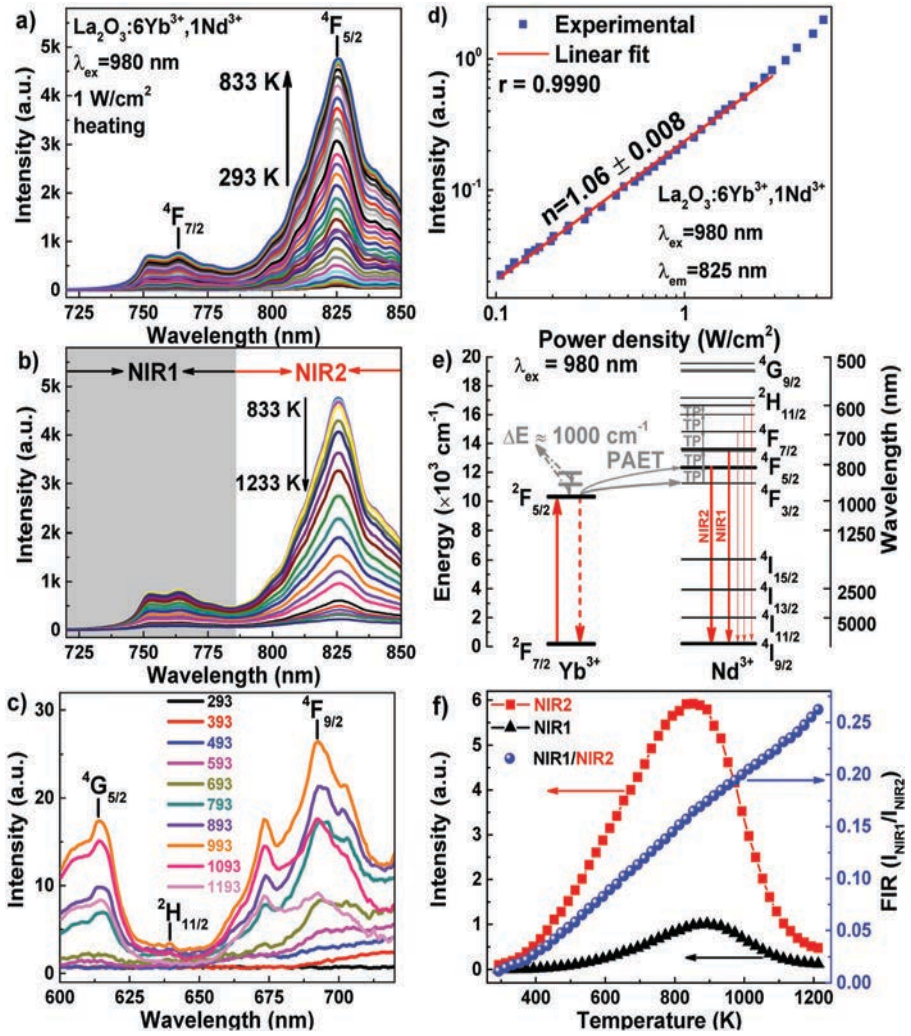

Fig. 2 Temperature dependent UC emission spectra of La_2O_3:6Yb^{3+},1Nd^{3+} for the temperature range of (a) 293 833 and (b) 833 1233 K with a step of 20 K under excitation of a 980 nm LD with a power density of 1 W cm ^{2}. (c) Magnified view of temperature dependent UC emission spectra in the spectral region of 600 720 nm by a factor of ×200. Labels in (a and c) represent the transitions of Nd^{3+} from the labelled excited states to ground sates of $^4I_{9/2}$. The new background was taken at the beginning of each measurement. (d) Double logarithmic plot of UC emission intensity of Nd^{3+} at 825 nm dependent on the excitation power density of 0.1 6 W cm ^{2}. Red solid line in (d) is the linear fit of the experimental data. (e) Schematic draw of the energy level diagram of Yb^{3+} and Nd^{3+}, and mechanisms of UC emission and TP under excitation of 980 nm LD. PAET and TP represents phonon assisted energy transfer and thermal population, respectively. (f) Variation of the integrated emission intensity of NIR1 (black triangle), NIR2 (red square) and FIR of NIR1/NIR2 (blue sphere) as a function of temperature over temperature range of 293 1233 K with a step of 20 K.

regime of 0.1–3 W cm^{-2}, a slope value of 1.06 ± 0.01 can be obtained by the linear fitting of the double-logarithmic plot. This indicates that a single photon process of phonon-assisted Nd^{3+} UC emission under 980 nm excitation is occurring, which will be discussed later in detail. For the high power density regime of >3 W cm^{-2}, a higher slope value can be observed, which may be linked to self-heating induced *via* the LD excitation.

Fig. 2e schematically shows UC emission and TP mechanisms of La_2O_3:6Yb^{3+},1Nd^{3+}. Under 980 nm excitation, electrons are pumped from Yb^{3+}:$^2F_{7/2}$ to Yb^{3+}:$^2F_{5/2}$. An energy gap ΔE of ~1000 cm^{-1} between energy levels of Yb^{3+}:$^2F_{7/2}$ and Nd^{3+}:$^2F_{3/2}$ can be observed. From our former study, we know that the phonon energy of La_2O_3 is ~450 cm^{-1} and thus ~2–3 phonons are required to enable the energy transfer (ET) from Yb^{3+}:$^2F_{7/2}$ to Nd^{3+}:$^2F_{3/2}$ by phonon-annihilation.[52] This process is frequently reported as phonon-assisted energy transfer (PAET) in co-doped materials such as Yb^{3+}/Nd^{3+}.[24,38–40,52] The almost linear process of Nd^{3+} emission with excitation power density (Fig. 2d) supports the PAET UC mechanism observed for Yb^{3+}/Nd^{3+} in La_2O_3. The ΔE value of $^4F_{3/2}$/$^4F_{5/2}$ and $^4F_{5/2}$/$^4F_{7/2}$ is ~1000 cm^{-1} and these levels are strongly thermally coupled. Consequently, the TP between these levels leads to the intense emission from Nd^{3+}:$^4F_{7/2}$ and Nd^{3+}:$^4F_{5/2}$ levels with maxima at 765 and 825 nm (Fig. 2a and b). For the higher lying levels of Nd^{3+}:$^4F_{9/2}$, Nd^{3+}:$^2H_{11/2}$ and Nd^{3+}:$^4G_{5/2}$, only faint emission from these levels can be observed at high temperature (>593 K), as shown in Fig. 2c. Due to the much higher energy of these levels with respect to Nd^{3+}:$^4F_{3/2}$, many more phonons (>5) are required to bridge the gap. Thus, the emission from these levels is only possible at high temperature and has to compete with the thermal quenching effect.

Fig. 2f summarizes dependence of integrated emission intensity of NIR1 and NIR2, and FIR of NIR1/NIR2 at a temperatures step of 20 K. Importantly, both NIR1 and NIR2 only exhibit very weak thermal quenching effect with temperature.

Due to the effective TP between Nd^{3+}:$^2F_{5/2}$ and Nd^{3+}:$^2F_{3/2}$, the emission intensity of NIR2 strongly increases with temperatures up to 853 K. At 853 K, it has increased ~60 times with respect to the initial intensity at 293 K. Higher temperatures (>853 K) leads to the decrease of emission intensity of NIR2. However, at 1233 K it remains four times stronger than that at 293 K. It is noteworthy that the blackbody radiation at high temperature regime (>1200 K) slightly decreases the certainty to which NIR2 can be measured. Similarly, NIR1 significantly increases with temperatures, but to a much greater degree than NIR2 due to the effective TP between Nd^{3+}:$^2F_{7/2}$ and Nd^{3+}:$^2F_{5/2}$. At 893 K, a maximum gain factor of 900-fold can be observed with respect to the initial emission intensity at 293 K. The slightly higher emission maximum temperature of NIR1 (893 K) than NIR2 (853 K) is ascribed to the TP between Nd^{3+}:$^2F_{7/2}$ and Nd^{3+}:$^2F_{5/2}$. It is noteworthy that the emission intensity of NIR1 and NIR2 below room temperature become too weak to be well resolved with an excitation power density of 1 W cm^{-2}, thus performance at less than room temperature is not reported here. The high thermal quenching temperature of La_2O_3:6Yb^{3+},1Nd^{3+} (853 K for NIR1) and (893 K for NIR2) is among the highest reported value for Yb^{3+}/Nd^{3+} co-doped UC emission. This unique features allows the accurate thermometry over a wide temperature range,[7] being much broader than that of Yb^{3+}/Er^{3+} UC materials.[4,7] Consequently, the FIR of NIR1/NIR2 significantly increases with temperature from 0.01 (293 K) to 0.26 (1233 K). The large change of FIR of NIR1/NIR2 enables its application in FIR thermometers.

The emission intensity for a given excited state with temperature can be described by eqn (1):[16,53]

$$I \propto gAh\nu \cdot \exp\left(\frac{E}{k_B T}\right), \quad (1)$$

where, g, A, h, ν, E, k_B and T are the degeneracy of the state, the spontaneous emission rate, the Planck constant, the frequency, the energy of the level, the Boltzmann constant and the absolute temperature, respectively. The FIR of two TCLs follows Boltzmann distribution and can be described by eqn (2):[16]

$$\mathrm{FIR} = \frac{I_2}{I_1} = \frac{g_2 A_2 h\nu_2}{g_1 A_1 h\nu_1} \exp\left(\frac{\Delta E_{21}}{k_B T}\right) = C \exp\left(\frac{\Delta E_{21}}{k_B T}\right), \quad (2)$$

where, I_2 and I_1 are the fluorescence intensity of upper and lower levels of two TCLs; C is the temperature-independent scaling constant; and ΔE_{21} is the energy gap between the TCLs.[16] For the present case, Nd^{3+}:$^2F_{7/2}$ and Nd^{3+}:$^2F_{5/2}$ is the upper and lower level of TCLs, respectively.

The energy gap ΔE between TCLs can be obtained by fitting of experiment data of FIR *via* eqn (2). The best fitting of experimental FIR (NIR1/NIR2) data is plotted in Fig. 3a. The fitting quality is high with r^2 = 0.9996. The fitted energy gap (ΔE_f) value of 927 cm^{-1} is very close to the experimental energy gap (ΔE_m) of 950 cm^{-1}, which is determined from DRS (refer Fig. 1d). The error δ between ΔE_f and ΔE_m is given by eqn (3):[7]

$$\delta = \frac{|\Delta E_m \quad \Delta E_f|}{\Delta E_m} \times 100\%, \quad (3)$$

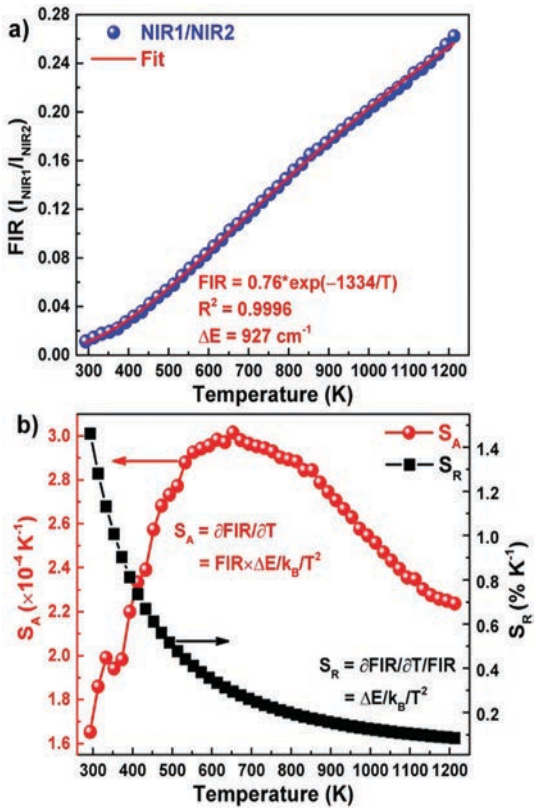

Fig. 3 Variation of (a) FIR and (b) absolute (S_A) and relative temperature sensitivity (S_R) dependent on temperature. Red solid line in (a) is the best fit of experimental data (blue sphere) by equation of FIR = $C \times \exp(\ \Delta E/k_B/T)$. Lines in (b) are guides for the eyes.

where δ is determined to be as small as ~2%. The absolute temperature sensitivity (S_A) is defined as the absolute FIR change with temperature variation and can be calculated using eqn (4):

$$S_A = \mathrm{FIR} \times \frac{\Delta E}{k_B T^2}. \quad (4)$$

From eqn (4), we can see that S_A depends on absolute FIR value and it is not suitable for the fair comparison among different systems.[1] Recently, relative temperature sensitivity (S_R) – which is defined as the ratio of S_A and FIR – has been frequently used as a standard parameter to quantitative comparison of temperature sensitivity of different systems. It is the normalized change in FIR with temperature variation and is calculated using eqn (5):[11,20]

$$S_R = \frac{1}{\mathrm{FIR}} \times \frac{\partial \mathrm{FIR}}{\partial T} = \frac{\Delta E}{k_B T^2}. \quad (5)$$

Furthermore, T_{max}, which is defined as the temperature where the maximum S_A obtained can be evaluated as follows:[54]

$$\frac{\partial^2 \mathrm{FIR}}{\partial^2 T} = \mathrm{FIR} \times \left(\frac{\Delta E}{k_B T_{max}{}^3} \quad 2\right) \times \frac{\Delta E}{k_B T_{max}{}^3} = 0 \quad (6)$$

$$T_{max} = \frac{\Delta E}{2K_B} \quad (7)$$

Thus, the large ΔE value facilitates the large T_{max} value. T_{max} is calculated to be 667 K. The high T_{max} value favours for the high temperature sensitivity at high temperature.

Table 1 Comparisons of thermometer parameters of Yb^{3+}/Nd^{3+} and Yb^{3+}/Er^{3+} doped UC host materials including TCLs, temperature range, ΔE and S_R. GC and CS represents glass ceramic and core/shell materials, respectively

Materials	TCLs	Temperature range (K)	ΔE (cm ^{1})	S_R (K ^{1})	Ref.
La_2O_3:Yb^{3+},Nd^{3+}	Nd^{3+}:$^2F_{7/2}$,$^2F_{5/2}$	293 1233	927	$1334/T^2$	This work
$NaYF_4$:Yb^{3+},Nd^{3+}	Nd^{3+}:$^2F_{7/2}$,$^2F_{5/2}$	303 873	895	$1288/T^2$	40
$CaWO_4$:Yb^{3+},Nd^{3+}	Nd^{3+}:$^2F_{7/2}$,$^2F_{5/2}$	297 420	889	$1459/T^2$	39
GC:Yb^{3+},Nd^{3+}	Nd^{3+}:$^2F_{7/2}$,$^2F_{5/2}$	303 623	1310	$1885/T^2$	23
K_3LuF_6:Yb^{3+},Er^{3+} GC	Er^{3+}:$^2H_{11/2}$,$^2S_{3/2}$	300 773	870	$1256/T^2$	55
$CaMoO_4$:Yb^{3+},Er^{3+}	Er^{3+}:$^2H_{11/2}$,$^2S_{3/2}$	300 513	829	$1193/T^2$	56
La_2O_2S:Yb^{3+},Er^{3+}	Er^{3+}:$^2H_{11/2}$,$^2S_{3/2}$	294 562	794	$1143/T^2$	57
$NaYF_4$:Yb^{3+},Er^{3+}	Er^{3+}:$^2H_{11/2}$,$^2S_{3/2}$	298 318	714	$1028/T^2$	58
$NaYF_4$:Yb^{3+},Er^{3+}/SiO_2 CS	Er^{3+}:$^2H_{11/2}$,$^2S_{3/2}$	300 900	716	$1031/T^2$	59
YF_3:Yb^{3+},Er^{3+}	Er^{3+}:$^2H_{11/2}$,$^2S_{3/2}$	260 490	688	$997/T^2$	20
$NaY(MoO_4)_2$:Yb^{3+},Er^{3+}	Er^{3+}:$^2H_{11/2}$,$^2S_{3/2}$	303 523	683	$983/T^2$	60
Y_2O_3:Yb^{3+},Er^{3+}	Er^{3+}:$^2H_{11/2}$,$^2S_{3/2}$	93 613	616	$886/T^2$	61
$Y_2Ti_2O_7$:Yb^{3+},Er^{3+}	Er^{3+}:$^2H_{11/2}$,$^2S_{3/2}$	298 673	564	$812/T^2$	62
YVO_4:Yb^{3+},Er^{3+}	Er^{3+}:$^2H_{11/2}$,$^2S_{3/2}$	302 483	538	$774/T^2$	63

The variation of the S_A and S_R value with temperature from 293 to 1233 K is illustrated in Fig. 3b. The S_A value slightly increases with temperature from 1.6×10^{-4} K^{-1} at 293 K to the maximum 3.0×10^{-4} K^{-1} at 693 K. The higher temperature slightly decreases from 3.0×10^{-4} K^{-1} at 693 K to 2.2×10^{-4} K^{-1} at 1233 K. The maximum S_A located in the region of the strongest emission intensity of NIR1 and NIR2, which enables the high sensing accuracy at high temperature. The S_R value is determined to be $1334/T^2$. In the studied temperature region (293–1233 K), the maximum S_R value is 1.6% K^{-1} at the lowest measuring temperature of 293 K and it decreases with temperature from 1.6% K^{-1} at 293 K to 0.1% K^{-1} at 1233 K. S_R value is comparable with other reported values for Yb^{3+}/Nd^{3+} doped UC materials and is higher than the frequently reported Yb^{3+}/Er^{3+} co-doped UC materials, as summarized in Table 1.

Repeatability tests over four heating and cooling cycles (temperature range of 293–1233 K with a step of 20 K) were conducted using the La_2O_3:Yb^{3+}/Nd^{3+} based FIR thermometer (see Fig. 4). From the overlay curves of all four heating and cooling cycles, we can clearly see the excellent repeatability of emission intensity of NIR1, NIR2, and the FIR of NIR1/NIR2. Time dependent emission intensity over 40 min by the step of 2 min at given temperature also confirms the excellent repeatability of emission intensity of NIR1 and NIR2, and FIR of NIR1/NIR2 with time, as shown in Fig. S1 (ESI†). Temperature uncertain ΔT_{min} is defined as the ratio of uncertainty and sensitivity. Thus, ΔT_{min} can be evaluated by the standard deviation (σ) and S_R using eqn (8):[18,64]

$$\Delta T_{min} = \frac{\sigma}{S_R}, \quad (8)$$

where σ is calculated in four independent heating and cooling cycles. Fig. 5 shows variation of σ, S_R and ΔT_{min} with temperature. At low temperature (<400 K), a low temperature uncertain

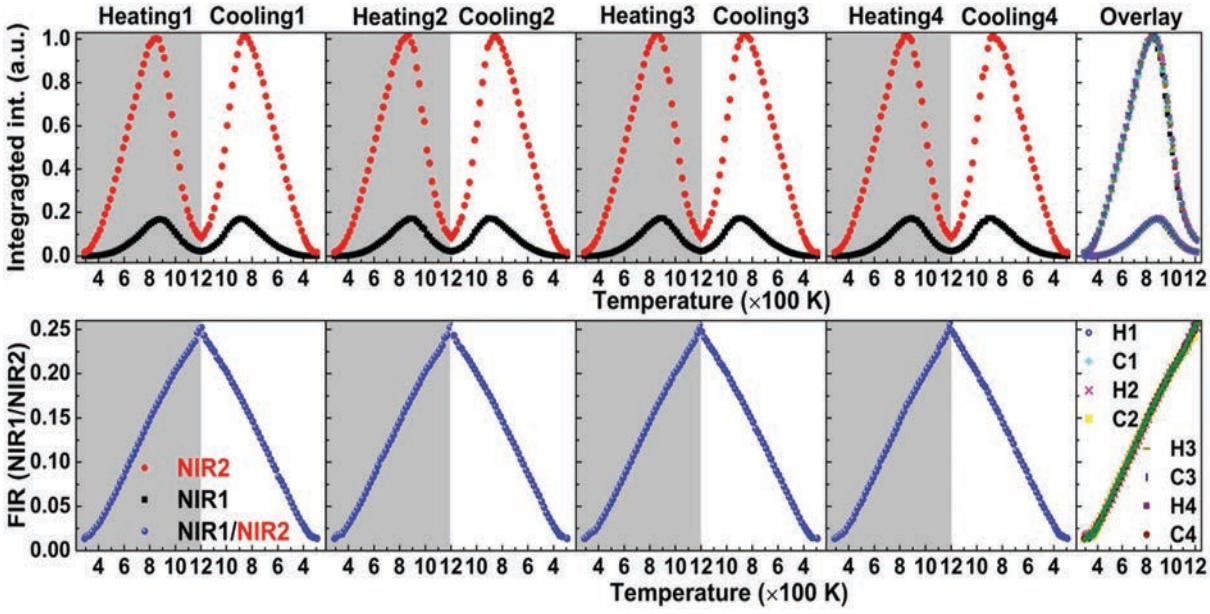

Fig. 4 Repeatability of integrated intensity of NIR1 and NIR2 (upper panels), and FIR of NIR1/NIR2 (lower panels) over 4 heating and cooling cycles from 293 to 1233 K with a step of 20 K. The last panel shows the overlay of the integrated intensity of NIR1, NIR2, and the FIR of NIR1/NIR2 for the 4 different heating and cooling cycles. H and C represent heating and cooling, respectively.

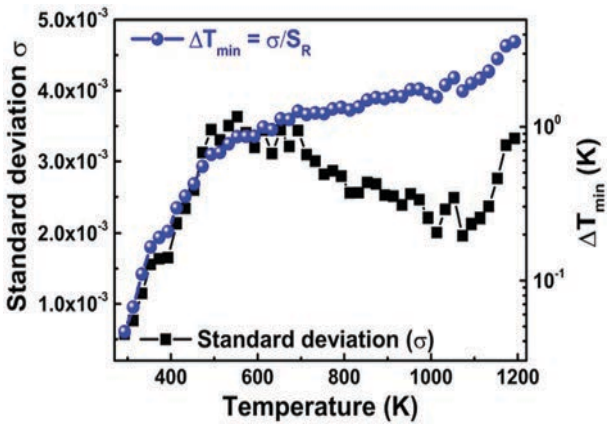

Fig. 5 Variation of standard deviation (σ) and temperature uncertain $\Delta T_{min} = \sigma/S_R$ as a function of temperature from 293 to 1233 K with a step of 20 K based on 4 heating and cooling cycles.

of 0.1 K can be obtained. For the temperature range of 400–850 K and 850–1233 K, temperature uncertain level of <1 and <3 K can be observed, respectively. The temperature uncertainty ΔT_{min} of La_2O_3:Yb^{3+},Nd^{3+} is comparable or even better than the reported values for the Yb^{3+}/Er^{3+} pair. For example, the ΔT_{min} value of 1–5 K is reported for $NaYF_4$:Yb^{3+},Er^{3+}/SiO_2 core/shell UC nanocrystals in the temperature range of 290–900 K.[16] The ΔT_{min} value of $\sim$0.3 K is reported for SrF_2:Yb^{3+},Er^{3+} UC nanoparticles in the temperature range of 303–373 K.[65]

Further performance enhancement of the FIR thermometers based in Yb^{3+}/Nd^{3+} co-doped La_2O_3 microcrystals is expected *via* the optimization of excitation sources, Yb^{3+}/Nd^{3+} doping concentrations, and synthesis conditions. These will be investigated in future work.

4. Conclusions

We report on Yb^{3+}/Nd^{3+} co-doped La_2O_3 microcrystals based NIR ratiometric thermometers operating from room temperature up to 1233 K. The energy gap ΔE value of TCLs of $^4S_{3/2}/^4F_{7/2}$ (NIR1) and $^4F_{5/2}$ (NIR2) is $\sim$950 cm^{-1} which is highly suitable for ratiometric thermometers. The emission intensity of NIR1 and NIR2 strongly increases with temperatures up to 893 and 853 K, respectively, due to the TP effects. The weak thermal quenching and high peak emission maximum temperature for TCLs of NIR1 and NIR2 afford high sensing accuracy and wide range temperature sensing. The FIR of NIR1/NIR2 significantly increase with temperature from 0.01 (293 K) to 0.26 (1233 K). The large change of FIR of NIR1/NIR2 enables its application in ratiometric thermometers. The relative sensitivity (S_R) value is determined to be $1334/T^2$. In the studied temperature region (293–1233 K), the maximum S_R value is 1.6% K^{-1} at 293 K and it decreases with temperature from 1.6% K^{-1} at 293 K to 0.1% K^{-1} at 1233 K. S_R value is comparable with other reported value for Yb^{3+}/Nd^{3+} doped UC materials and higher than the frequently reported Yb^{3+}/Er^{3+} co-doped UC materials. The excellent repeatability of emission intensity of NIR1, NIR2, and FIR of NIR1/NIR2 is confirmed by 4 independent heating and cooling cycles. A low temperature uncertain of 0.1 K, 1 and 3 K can be obtained for the temperature range of 293–400 K, 400–850 K and 850–1233 K, respectively. These combined features make them promising as ratiometric thermometers over a wide temperature range of 293–1233 K.

Conflicts of interest

There are no conflicts to declare.

Acknowledgements

The authors gratefully acknowledge financial support by the Helmholtz Association – *via* (i) the program Science and Technology of Nanosystems (STN); (ii) the Recruitment Initiative of Prof. B. S. Richards; (iii) the Helmoltz Materials Energy Foundry (HEMF); and (iv) the Helmholtz Energy Materials Characterization Platform (HEMCP) for funding the Bruker D8 – as well as the Technology Transfer Project N038 between KIT and Polysecure GmbH.

Notes and references

1 C. D. S. Brites, P. P. Lima, N. J. O. Silva, A. Millan, V. S. Amaral, F. Palacio and L. D. Carlos, *Nanoscale*, 2012, **4**, 4799–4829.
2 L. H. Fischer, G. S. Harms and O. S. Wolfbeis, *Angew. Chem., Int. Ed.*, 2011, **50**, 4546–4551.
3 V. K. Rai, *Appl. Phys. B*, 2007, **88**, 297–303.
4 X.-d. Wang, O. S. Wolfbeis and R. J. Meier, *Chem. Soc. Rev.*, 2013, **42**, 7834–7869.
5 F. Zhang, in *Photon Upconversion Nanomaterials*, ed. F. Zhang, Springer Berlin Heidelberg, Berlin, Heidelberg, 2015, pp. 343–374.
6 B. R. Reddy, I. Kamma and P. Kommidi, *Appl. Opt.*, 2013, **52**, B33–B39.
7 X. Wang, Q. Liu, Y. Bu, C.-S. Liu, T. Liu and X. Yan, *RSC Adv.*, 2015, **5**, 86219–86236.
8 C. D. S. Brites, P. P. Lima, N. J. O. Silva, A. Millan, V. S. Amaral, F. Palacio and L. D. Carlos, *New J. Chem.*, 2011, **35**, 1177–1183.
9 Y. Gao, F. Huang, H. Lin, J. Zhou, J. Xu and Y. Wang, *Adv. Funct. Mater.*, 2016, **26**, 3139–3145.
10 B. Dong, B. Cao, Y. He, Z. Liu, Z. Li and Z. Feng, *Adv. Mater.*, 2012, **24**, 1987–1993.
11 M. Back, E. Trave, J. Ueda and S. Tanabe, *Chem. Mater.*, 2016, **28**, 8347–8356.
12 J. Cao, X. Li, Z. Wang, Y. Wei, L. Chen and H. Guo, *Sens. Actuators, B*, 2016, **224**, 507–513.
13 P. Cortelletti, C. Facciotti, I. X. Cantarelli, P. Canton, M. Quintanilla, F. Vetrone, A. Speghini and M. Pedroni, *Opt. Mater.*, 2017, **68**, 29–34.
14 B. Dong, D. P. Liu, X. J. Wang, T. Yang, S. M. Miao and C. R. Li, *Appl. Phys. Lett.*, 2007, **90**, 181117.
15 G. Gao, S. Krolikowski, M. Peng and L. Wondraczek, *J. Lumin.*, 2016, **180**, 234–240.
16 R. G. Geitenbeek, P. T. Prins, W. Albrecht, A. van Blaaderen, B. M. Weckhuysen and A. Meijerink, *J. Phys. Chem. C*, 2017, **121**, 3503–3510.

17 L. Liu, Y. Wang, X. Zhang, K. Yang, Y. Bai, C. Huang and Y. Song, *Opt. Commun.*, 2011, **284**, 1876–1879.
18 D. D. Miroslav, *Methods Appl. Fluoresc.*, 2016, **4**, 042001.
19 H. Suo, F. Hu, X. Zhao, Z. Zhang, T. Li, C. Duan, M. Yin and C. Guo, *J. Mater. Chem. C*, 2017, **5**, 1501–1507.
20 H. Suo, X. Zhao, Z. Zhang, T. Li, E. M. Goldys and C. Guo, *Chem. Eng. J.*, 2017, **313**, 65–73.
21 R. K. Verma and S. B. Rai, *J. Quant. Spectrosc. Radiat. Transfer*, 2012, **113**, 1594–1600.
22 W. Xu, H. Zhao, Y. Li, L. Zheng, Z. Zhang and W. Cao, *Sens. Actuators, B*, 2013, **188**, 1096–1100.
23 W. Xu, H. Zhao, Z. Zhang and W. Cao, *Sens. Actuators, B*, 2013, **178**, 520–524.
24 L. A. O. Nunes, A. S. Souza, L. D. Carlos and O. L. Malta, *Opt. Mater.*, 2017, **63**, 42–45.
25 S. Balabhadra, M. L. Debasu, C. D. S. Brites, L. A. O. Nunes, O. L. Malta, J. Rocha, M. Bettinelli and L. D. Carlos, *Nanoscale*, 2015, **7**, 17261–17267.
26 G. Gao, A. Turshatov, I. A. Howard, D. Busko, R. Joseph, D. Hudry and B. S. Richards, *Adv. Sustainable Syst.*, 2017, **1**, 1600033.
27 S. Fan, S. Wang, L. Yu, H. Sun, G. Gao and L. Hu, *Opt. Express*, 2017, **25**, 180–190.
28 F. Auzel, *Chem. Rev.*, 2004, **104**, 139–173.
29 J. Zhou, Q. Liu, W. Feng, Y. Sun and F. Li, *Chem. Rev.*, 2015, **115**, 395–465.
30 F. Wang and X. Liu, *Chem. Soc. Rev.*, 2009, **38**, 976–989.
31 J. Zhao, X. Zheng, E. P. Schartner, P. Ionescu, R. Zhang, T.-L. Nguyen, D. Jin and H. Ebendorff-Heidepriem, *Adv. Opt. Mater.*, 2016, **4**, 1507–1517.
32 S. Han, R. Deng, X. Xie and X. Liu, *Angew. Chem., Int. Ed.*, 2014, **53**, 11702–11715.
33 X. Liu, C.-H. Yan and J. A. Capobianco, *Chem. Soc. Rev.*, 2015, **44**, 1299–1301.
34 F. Wang, R. Deng, J. Wang, Q. Wang, Y. Han, H. Zhu, X. Chen and X. Liu, *Nat. Mater.*, 2011, **10**, 968–973.
35 B. Zhou, B. Shi, D. Jin and X. Liu, *Nat. Nanotechnol.*, 2015, **10**, 924–936.
36 C. Li, S. Li, B. Dong, Z. Liu, C. Song and Q. Yu, *Sens. Actuators, B*, 2008, **134**, 313–316.
37 N. Rakov and G. S. Maciel, *Opt. Lett.*, 2014, **39**, 3767–3769.
38 L. J. Q. Maia, F. M. Faria Filho, V. Jerez, A. L. Moura and C. B. de Araujo, *J. Mater. Chem. C*, 2015, **3**, 11689–11696.
39 W. Xu, Q. Song, L. Zheng, Z. Zhang and W. Cao, *Opt. Lett.*, 2014, **39**, 4635–4638.
40 W. Xu, H. Qi, L. Zheng, Z. Zhang and W. Cao, *Opt. Lett.*, 2015, **40**, 5678–5681.
41 X. Tian, X. Wei, Y. Chen, C. Duan and M. Yin, *Opt. Express*, 2014, **22**, 30333–30345.
42 U. Rocha, C. Jacinto da Silva, W. Ferreira Silva, I. Guedes, A. Benayas, L. Martínez Maestro, M. Acosta Elias, E. Bovero, F. C. J. M. van Veggel, J. A. García Solé and D. Jaque, *ACS Nano*, 2013, **7**, 1188–1199.
43 D. Wawrzynczyk, A. Bednarkiewicz, M. Nyk, W. Strek and M. Samoc, *Nanoscale*, 2012, **4**, 6959–6961.
44 G. Gao, D. Busko, S. Kauffmann-Weiss, A. Turshatov, I. A. Howard and B. S. Richards, *J. Mater. Chem. C*, 2017, **5**, 11010–11017.
45 B. Wu, M. Zinkevich, F. Aldinger, D. Wen and L. Chen, *J. Solid State Chem.*, 2007, **180**, 3280–3287.
46 R. D. Shannon, *Acta Crystallogr., Sect. A: Cryst. Phys., Diffr., Theor. Gen. Crystallogr.*, 1976, **32**, 751–767.
47 G. J. Gao, M. Y. Peng and L. Wondraczek, *J. Mater. Chem. C*, 2014, **2**, 8083–8088.
48 G. J. Gao and L. Wondraczek, *J. Mater. Chem. C*, 2013, **1**, 1952–1958.
49 G. J. Gao and L. Wondraczek, *Opt. Mater. Express*, 2013, **3**, 633–644.
50 R. I. Epstein, M. I. Buchwald, B. C. Edwards, T. R. Gosnell and C. E. Mungan, *Nature*, 1995, **377**, 500–503.
51 B. Zhong, J. Yin, Y. Jia, L. Chen, Y. Hang and J. Yin, *Opt. Lett.*, 2014, **39**, 2747–2750.
52 A. F. Silva, F. Elan, E. L. Falcao-Filho, L. J. Q. Maia and C. B. de Araujo, *J. Mater. Chem. C*, 2017, **5**, 1240–1246.
53 C. D. S. Brites, A. Millán and L. D. Carlos, Lanthanides in Luminescent Thermometry, in *Handbook on the Physics and Chemistry of Rare Earths*, ed. J.-C. Bunzli and V. K. Pecharsky, Elsevier, 2016, ch. 281, pp. 339–427.
54 F. Huang, Y. Gao, J. Zhou, J. Xu and Y. Wang, *J. Alloys Compd.*, 2015, **639**, 325–329.
55 J. Cao, F. Hu, L. Chen, H. Guo, C. Duan and M. Yin, *J. Am. Ceram. Soc.*, 2017, **100**, 2108–2115.
56 S. Sinha, M. K. Mahata, H. C. Swart, A. Kumar and K. Kumar, *New J. Chem.*, 2017, **41**, 5362–5372.
57 Y. Yang, C. Mi, F. Yu, X. Su, C. Guo, G. Li, J. Zhang, L. Liu, Y. Liu and X. Li, *Ceram. Int.*, 2014, **40**, 9875–9880.
58 F. Vetrone, R. Naccache, A. Zamarrón, A. Juarranz de la Fuente, F. Sanz-Rodríguez, L. Martinez Maestro, E. Martín Rodriguez, D. Jaque, J. García Solé and J. A. Capobianco, *ACS Nano*, 2010, **4**, 3254–3258.
59 R. G. Geitenbeek, P. T. Prins, W. Albrecht, A. van Blaaderen, B. M. Weckhuysen and A. Meijerink, *J. Phys. Chem. C*, 2017, **121**, 3503–3510.
60 T. Wen, Y. Zhou, Y. Guo, C. Zhao, B. Yang and Y. Wang, *J. Mater. Chem. C*, 2016, **4**, 684–690.
61 P. Du, L. Luo, Q. Yue and W. Li, *Mater. Lett.*, 2015, **143**, 209–211.
62 B. P. Singh, A. K. Parchur, R. S. Ningthoujam, P. V. Ramakrishna, S. Singh, P. Singh, S. B. Rai and R. Maalej, *Phys. Chem. Chem. Phys.*, 2014, **16**, 22665–22676.
63 M. K. Mahata, K. Kumar and V. K. Rai, *Sens. Actuators, B*, 2015, **209**, 775–780.
64 M. Quintanilla, A. Benayas, R. Naccache and F. Vetrone, *Thermometry at the Nanoscale: Techniques and Selected Applications*, The Royal Society of Chemistry, 2016, pp. 124–166.
65 S. Balabhadra, M. L. Debasu, C. D. S. Brites, R. A. S. Ferreira and L. D. Carlos, *J. Phys. Chem. C*, 2017, **121**, 13962–13968.

----- Supporting Information -----

Wide-range non-contact fluorescence intensity ratio thermometer based on Yb^{3+}/Nd^{3+} co-doped La_2O_3 microcrystals operating from 290 to 1230 K

Guojun Gao[1*], Dmitry Busko[1], Sandra Kauffmann-Weiss[2], Andrey Turshatov[1], Ian A. Howard[1,3] and Bryce S. Richards[1,3*]

[1] Institute of Microstructure Technology, Karlsruhe Institute of Technology, 76344 Eggenstein-Leopoldshafen, Germany

[2] Institute of Technical Physics, Karlsruhe Institute of Technology, 76344 Eggenstein-Leopoldshafen, Germany

[3] Light Technology Institute, Karlsruhe Institute of Technology, Engesserstrasse 13, 76131 Karlsruhe, Germany

[*] Corresponding authors: Dr. G. Gao: guojun.gao@kit.edu; Prof. B.S. Richards: bryce.richards@kit.edu

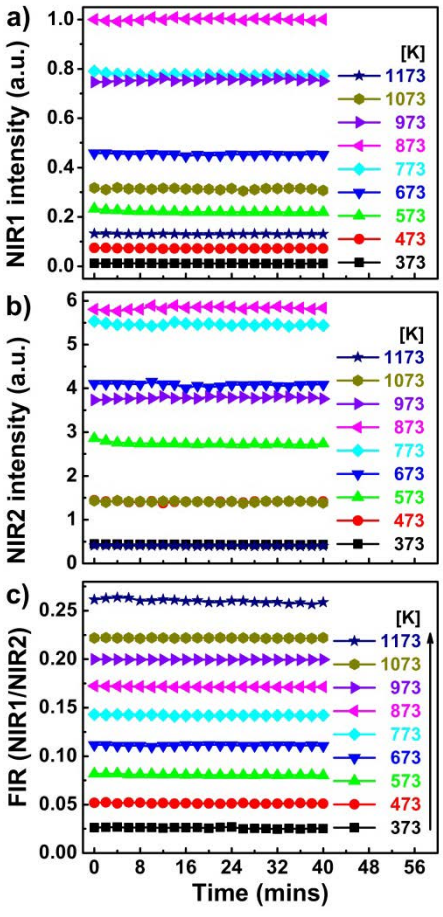

Figure **S1**. Repeatability of integrated intensity of a) NIR1 and b) NIR2, and c) FIR of NIR1/NIR2 with time over 40 mins at varies temperatures.